

Learning 3D Dense Correspondence via Canonical Point Autoencoder

An-Chieh Cheng¹, Xueting Li², Min Sun¹, Ming-Hsuan Yang², Sifei Liu³,
¹National Tsing-Hua University ²University of California, Merced, ³NVIDIA

Abstract

We propose a canonical point autoencoder (CPAE) that predicts dense correspondences between 3D shapes of the same category. The autoencoder performs two key functions: (a) encoding an arbitrarily ordered point cloud to a canonical primitive, e.g., a sphere, and (b) decoding the primitive back to the original input instance shape. As being placed in the bottleneck, this primitive plays a key role to map all the unordered point clouds on the canonical surface and to be reconstructed in an ordered fashion. Once trained, points from different shape instances that are mapped to the same locations on the primitive surface are determined to be a pair of correspondence. Our method does not require any form of annotation or self-supervised part segmentation network and can handle unaligned input point clouds. Experimental results on 3D semantic keypoint transfer and part segmentation transfer show that our model performs favorably against state-of-the-art correspondence learning methods.

1 Introduction

With prior knowledge and experience, humans can easily perceive corresponding object parts (e.g., the wings from two different airplanes), understand their shape and appearance variance, in order to distinguish different objects coming from the same category. In computer vision, modeling dense correspondence between 3D shapes in one category is fundamental for numerous applications, such as robot grasping [1, 2], object manipulation [3] and texture mapping [4, 2]. However, existing 3D cameras typically capture raw point clouds of shape surfaces that are arbitrarily-ordered and unstructured, in which correspondences are not established. 3D mesh representation, although is usually parameterized with UV maps that can indicate correspondences, cannot be directly obtained from sensors and needs to be reconstructed from other types of representations, e.g., 2D images [5, 6] or 3D point clouds [7]. In this work, we focus on learning point cloud correspondences, which remains an open challenge since it is infeasible to label ground truth correspondence annotations.

Without ground truth annotations, existing methods mainly discover shape correspondences via seeking a form of canonical space that can associate various instance shapes. For example, in particular shape domains such as human bodies [8] and human faces [9], parameterized shape primitives have been designed to fit the observed raw data and to obtain the correspondences. Such designs, however, cannot be generalized to other categories, e.g., man-made objects [10]. Recently, several part co-segmentation networks relax the requirements of specific parameterized primitives, but instead decompose input shapes into an ordered group of simplest part constitutions [11, 12], in a self-supervised manner. These methods, however, require careful selection of the autoencoder architectures (i.e., they need to be considerably shallow to let the branches only able to represent simple shapes), and the number of part bases. Moreover, such part-based representation does not explicitly provide fine-grained (e.g., point-level) correspondences.

In this work, we introduce a novel canonical space where dense (i.e., point-level) correspondences for all the shapes of a category can be explicitly obtained from. Inspired by 3D mesh representation [13, 14, 15, 5] where shapes from one category are represented as deformations on top of a shape

primitive, in our work, we set the canonical space as a 3D UV sphere. Our goal is to learn a “point cloud-to-sphere mapping” such that corresponding parts from different instances overlap when mapped onto the canonical sphere. In other words, similar to the mesh representation, a unique UV coordinate can represent the same semantic point/local region of shapes (e.g., the tip of an aeroplane’s wing), regardless of shape variations. Towards this goal, we introduce the canonical point autoencoder (CPAE): we place the sphere primitive at the bottleneck; the encoder non-linearly maps each individual input shape to the sphere primitive, where the decoder deforms the primitive back to match the original shape. We show that with several self-supervised objectives, this autoencoder architecture effectively (1) enforces the input points warped to the surface of the sphere primitives, and (2) encourages those corresponding points from different instances mapped to the same location on the sphere – both guarantee that the network learns correct dense correspondences. Essentially, we *do not* assume all object shapes in one category having the same topology, e.g., an armchair does not have correspondence on its armrests, with another instance without an armrest. To introduce such uncertainty for correspondence matching, we propose an adaptive Chamfer loss on the bottleneck to allow customized primitive for each instance. As such, we are able to determine if a point on one instance has a correspondence in another point cloud.

One advantage of the proposed method compared to the recent work [12] is that we can learn correspondences even when instances in the training dataset are not aligned, i.e., our model is rotation-invariant within a certain rotation range and does not need to predict an additional rotation matrix as used in [12]. The main contributions of this work are:

- We introduce a novel canonical space – a UV sphere, that explicitly represents dense correspondences of shapes from one category.
- With the canonical space on the bottleneck, we design an autoencoder that learns such a “point cloud-to-sphere mapping” via a group of self-supervised objectives.
- We apply the proposed method on various categories and quantitatively evaluate on the task of 3D semantic keypoint transfer and part segmentation label transfer, achieving comparable if not better performance than state-of-the-art methods.

2 Related Work

Deep Learning on Point Clouds. As a flexible and memory efficient representation of 3D shapes, point cloud has been widely studied and combined with deep neural networks. The PointNet [16] solves point cloud classification and segmentation by using MLPs and a max pooling layer to aggregate 3D shape information. One crucial property of the PointNet is that it is able to handle unordered input and is thus invariant to point permutations. In our work, we utilize the first few layers of the PointNet as our shape encoder. Another line of works [17, 18, 19, 20] focus on reconstructing or generating point clouds. The most representative and related to our work is the FoldingNet [17], where a point cloud is first encoded by a graph-based encoder and then reconstructed by sequentially applying the “folding operation” (instantiated by MLPs) to a 2D UV map. In this work, we reveal why the MLPs are able to preserve point order and utilize it as building blocks in our CPAE.

3D Dense Correspondence. Given a pair of source and target instance in the same category, 3D dense correspondence learning targets at finding a corresponding point in the target instance for each point from the source instance. Several approaches [21, 22, 23] resolve this task through point cloud registration, using labeled pairwise correspondence as supervision. To relax constraints on supervision, Bhatnagar et al. [24] predict part correspondences to a template via implicit functions. Unfortunately, they require part labels for training. To unsupervisedly learn 3D dense correspondence, Chen et al. [25] propose a method to learn 3D structure points that are consistent across different instances. However, the model assumes structure similarity among different instances, which ignores intra-class variants and fails to detect non-existing correspondences between dissimilar shapes in the same category. Most relevant to our work, Liu et al. [12] introduce an unsupervised approach that leverages part features learned by the BAE-NET [11] to build dense correspondences. Their algorithm is feasible to calculate a confidence score representing the probability of correspondence. However, in order to train the implicit function, they require additional knowledge of object surface to compute the occupancy. Moreover, the correspondence learning in [12] heavily relies on the completeness of the part features from the BAE-NET [11], which can lead to incorrect correspondences for parts that BAE-NET cannot separate (e.g., flat surfaces, objects with fine-grained details). In contrast, our approach directly learns dense correspondences from the point cloud with self-supervision.

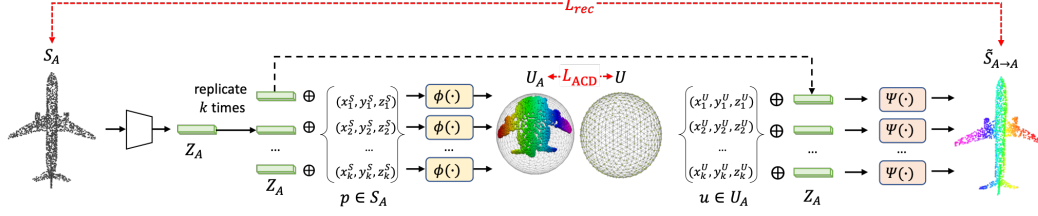


Figure 1: Overview of the proposed method. Here, $p = (x_i^S, y_i^S, z_i^S)$ is a point on the input point cloud S_A , $u = (x_i^U, y_i^U, z_i^U)$ is a point on the primitive U_A . The “ \oplus ” sign indicates concatenation. $\Phi(\cdot)$ and $\Psi(\cdot)$ are MLPs as discussed in Section 3.1.

3D Deformable Mesh Representations. Our algorithm is also related to methods [13, 14, 15, 5] that represent instance shapes as mesh deformations of a mesh primitive, i.e. a sphere template. Vertices on each instance surface that are mapped to the same locations on the shape primitive are discovered as correspondences. One obvious limitation is that only genus 0 shapes, e.g., birds [13, 5] can be deformed from a mesh sphere. In contrast, ours does not have such restriction thanks to the proposed non-linear mappings, instead of explicit deformation.

3 Proposed Method

In this section, we introduce our end-to-end CPAE for learning dense correspondences from point clouds without ground truth annotation. Given a point cloud S_A with individual point $p \in \mathbb{R}^3$ (see Figure 1), our model: (1) predicts its canonical primitive U_A (a “deformed” point cloud with the same number of points as S_A), which is supposed to be as close as possible to the canonical sphere in the bottleneck; (2) reconstructs the original input point cloud back from U_A . We show that while the first ensures each input point cloud to be warped to the surface of the sphere primitive, the second indirectly encourages the corresponding points from different point cloud instances to overlap during mapping to the primitive. In the following, we first describe our network architecture, i.e., the encoder and decoder modules. We then introduce the adaptive Chamfer loss and the reconstruction losses that are applied to each individual module. Finally, we show that our decoder reconstructs ordered point clouds, i.e., different point cloud instances can fetch their correspondences directly via the point indices, which provides a more accurate inference.

3.1 Network Architecture

Our method learns two mapping functions: one maps each individual 3D point $p \in \mathbb{R}^3$ in the world coordinates to the canonical space $\Phi(p) = u, u \in \mathbb{R}^3$, while the other conducts the inverse mapping $\Phi^{-1}(u) = p$. Instead of using a reversible network, we instantiate $\Phi(\cdot)$ and $\Phi^{-1}(\cdot)$ with two MLPs respectively, and cascade them to construct an autoencoder (i.e., $\Phi(\cdot)$ is the encoder and $\Psi(\cdot) \approx \Phi^{-1}(\cdot)$ is the decoder). However, this mapping function cannot be generalized to different point clouds if it only receives the coordinate of a single point p as the input. Therefore, we formulate them as conditional mapping functions by concatenating the input with a shape latent code Z_A that represents a unique input shape S_A , e.g., $\Phi(p, Z_A)$, in order to generalize the mapping functions to all instances in the same category.

There are three key modules in the proposed method: (1) a PointNet encoder that produces the shape latent code; (2) an encoder MLP (denoted as *canonical mapping*) that maps a point cloud to a primitive sphere, and (3) a decoder MLP (denoted as *inverse mapping*) that deforms the primitive sphere back to the input point cloud.

PointNet Encoder. As shown in Figure 1, given a point cloud $S_A \in \mathcal{R}^{k \times 3}$ with k points, we encode it using a PointNet [16] encoder in a way similar to [18, 8, 19]. Each 3D point of the input point cloud is represented as a 512 dimensional vector using an MLP with 3 hidden layers of 64, 128, 512 neurons and ReLU activations. We then aggregate all point features with max-pooling and a linear layer to generate a global latent code $z_A \in \mathcal{R}^{512}$. We use PointNet because it produces a robust latent code representing the global shape, which is also invariant to input permutation.

Canonical Mapping $\Phi(\cdot)$. To learn the canonical mapping function, we concatenate each point with the global latent code $[p, Z] \in \mathbb{R}^{515}$ as input to the MLP, which then outputs a 3D coordinate

$u \in \mathbb{R}^3$ in the canonical space. We construct a sphere point cloud by uniformly sampling a large number of points from a standard sphere mesh, and place them as the canonical primitive at the bottleneck. A Chamfer loss is used to measure the difference between the outputted point u and primitive to encourage the mapped point adhering to the surface (see Eq. (1)).

Ideally, all the mapped instances from the same category should be as close as possible to the canonical sphere primitive. However, an instance may include parts/regions that do not exist in other instances due to intra-class variation, e.g., not all chairs include armrests. With a conventional Chamfer loss, the shapes for objects with rare components do not converge during training, i.e., those rare components are mapped to locations that are far away from the primitive surface. Thus, we relax the bidirectional constraint of the Chamfer loss and allow each instance to produce its own “instance primitive” to some extent (see U_A in Figure 1). This is formulated via an adaptive Chamfer loss L_{ACD} :

$$L_{ACD}(U_A, U) = \frac{1}{|U_A|} \sum_{p \in U_A} \min_{q \in U} \|p - q\|_2 + \alpha \frac{1}{|U|} \sum_{q \in U} \min_{p \in U_A} \|q - p\|_2 \quad (1)$$

where $\alpha \sim [0, 1]$ is an adaptive parameter indicating to what extent the predicted instance primitive should match a canonical sphere, U_A and U are the instance primitive and the canonical UV primitive (e.g., a 3D UV sphere), respectively. When $\alpha = 1$, L_{ACD} is equivalent to calculating the conventional Chamfer distance between the unfolded primitive and the canonical UV primitive. During training, α is initialized to 1 and gradually decreased to 0. This allows the canonical mapping to predict instance-aware primitive since the second term of the Chamfer loss no longer constraints the primitive to be consistent with a canonical sphere. In the experiments (see Section 4.5), we show that this design allows us to infer rare object components that have no correspondences in other instances since non-corresponding regions usually occupy a distinct area in the canonical space.

Inverse Mapping $\Psi(\cdot)$. Similarly, we utilize another MLP in the decoder, which receives the concatenation of one point from the bottleneck and the global shape code, i.e., $[u, Z] \in \mathbb{R}^{515}$, as the input. The function learns to map it back to its original world coordinate p , which can be fulfilled via a point-to-point reconstruction loss. We leverage an MSE loss L_{MSE} , a Chamfer distance L_{CD} and an Earth Mover Distance (EMD) L_{EMD} between the reconstruction \hat{S} and input point cloud P :

$$L_{rec}(P, \hat{S}) = \mu_1 L_{MSE}(P, \hat{S}) + \mu_2 L_{CD}(P, \hat{S}) + \mu_3 L_{EMD}(P, \hat{S}) \quad (2)$$

where μ_1, μ_2, μ_3 are the weights, and empirically determined, $\mu_1 = 1e3$, $\mu_2 = 1e1$, and $\mu_3 = 1$.

The inverse mapping bears some resemblance to the principle of FoldingNet [17], which adopts an MLP architecture to map one 2D coordinate together with a global shape representation to the 3D world¹. However, since FoldingNet does not have the forward mapping function as ours and the input points are untraceable, it needs to use a Chamfer loss, instead of a point-wise loss (Eq. (2)) as ours.

Align Canonical Mappings via Cross-Reconstruction. With the encoder and objective function, the canonical mapping is able to map the input points to the surface of the canonical primitive. However, even with the reconstruction loss (Eq. (2)), there is no guarantee that the corresponding points from different shape instances can be overlapped on the sphere – which is the key to learn dense correspondences. For instance, in Figure 1, while S_A is mapped to the frontal half of the sphere, it is likely that another shape S_B will be mapped to the rear half.

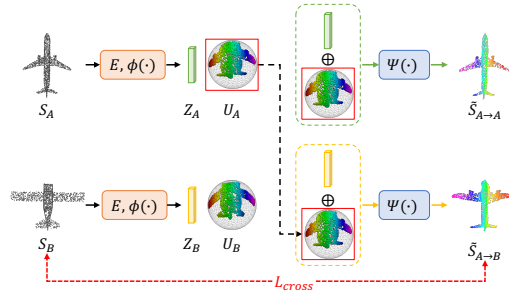


Figure 2: Cross-reconstruction. The $E, \Phi(\cdot), \Psi(\cdot)$ are identical as in Figure 1.

To better align the mapped points, we introduce a cross-structured decoder that leverages: (1) a self-reconstruction branch as presented in Eq. (2), and (2) a cross-reconstruction branch. As shown in Figure 2, we feed the combination of the predicted instance primitive U_A of point cloud S_A , with the shape latent vector Z_B of another randomly sampled point cloud S_B to the folding decoder. We then minimize the Chamfer distance between the output shape $\hat{S}_{A \rightarrow B}$ and S_B . The cross-reconstruction

¹Unlike our method, it utilizes and samples points from a standard 2D UV map instead of a 3D sphere.

loss between the point cloud S_A and S_B is:

$$L_{cross}(S_A, S_B) = L_{CD}(\hat{S}_{A \rightarrow B}, S_B) \quad (3)$$

The cross-reconstruction branch ensures even by swapping the predicted primitives U_A and U_B , the inverse mapping can still reconstruct their own shapes, conditioned on their own shape latent codes. That is, the decoder encourages U_A and U_B to overlap on the canonical primitive, and thus ensures the network learns correct correspondences.

Relation to Implicit Function. We note that since both mapping functions $\Phi(\cdot)$ and $\Psi(\cdot)$ process each input point independently, they can be interpreted as conditional implicit functions, which are widely applied for 3D shape reconstruction [26, 27], view synthesis [28, 29], and recently for self-supervised 3D correspondence [12]. Such an interpretation reveals that the MLPs indeed learn continuous mappings that are feasible for interpolations, e.g., once the decoder MLP is learned, it is able to map any point on a continuous sphere surface that is not necessarily among the mapped input u , to the world coordinate. E.g. one can sample points densely from the surface of the sphere to reconstruct a continuous surface or a 3D mesh.

3.2 Finding Correspondences from Ordered Point Clouds

In this section, we show that the CPAE is able to generate ordered point clouds (see the output point clouds in Figure 1). Compared to the methods obtaining correspondences by directly tracing overlapped points from the canonical space, our model that makes use of ordered output point cloud generates more accurate results during the inference stage.

Reconstruction of Ordered Point Clouds. We first show that an MLP [17] decoder preserves such correspondence, i.e. corresponding points outputted by the decoder are mapped from the same points on the canonical sphere. Given a point p_A on the source point cloud S_A , we denote its corresponding point on the target point cloud S_B as p_B and assume that they are decoded from two points u_A and u_B on the canonical sphere. A one-layer linear operation can be written as:

$$p_A = W \times u_A + b \quad \text{and} \quad p_B = W \times u_B + b \quad (4)$$

where W and b are learnable parameters instantiated as a fully-connected layer. Since Eq. (4) shows an affine transform, it implies that $p_A - p_B \propto u_A - u_B$. If $u_A \neq u_B$ and u_A is deformed to another point p'_B on shape S_B such that $p_A - p'_B < p_A - p_B$, which contradicts to the fact that p_B is the closest point to p_A among all points on S_B . Thus $u_A = u_B$, showing corresponding points are deformed from the same points on the canonical sphere.

Inference via CPAE. Given a source shape S_A and a query point $p_A \in S_A$, we target at searching the correspondence of the query point in a target shape S_B . We first compute the shape latent vectors for the two shapes as z_A and z_B . The query point is then mapped to a point u_A in the canonical space by the canonical mapping encoder. By feeding the concatenation of u_A and z_B to the inverse mapping decoder, we further map u_A to a point $p_{A \rightarrow B}$ on the reconstructed target shape $S_{A \rightarrow B}$. The correspondence of p_A (denoted as $p_B \in S_B$) is thus the closet point on S_B to $p_{A \rightarrow B}$.

Confidence of Correspondence. For each point and its correspondence pair (e.g. (p_A, p_B)), we can also compute a confidence score $C(p_A, p_B)$ to measure the confidence of this mapping:

$$C(p_A, p_B) = 1 - D(p_A, p_B) \quad (5)$$

where D refers to the normalized Euclidean distance between p_A and p_B in the 3D world coordinate. Similar to [12], if C is lower than a pre-defined threshold τ , we conclude that point p_A does not have a correspondence on shape S_B .

4 Experiments

In this section, we present evaluations of the proposed dense correspondence learning approach. To the best of our knowledge, there is no benchmark that provides ground-truth dense correspondences for general objects, which is exactly our motivation to learn dense correspondence with self-supervision. However, thanks to the learned dense correspondences across pairs of instances, we are able to carry out the task of 3D semantic keypoint transfer and part segmentation label transfer to evaluate the proposed method as in [12]. In the following, we first introduce our experimental setup as well

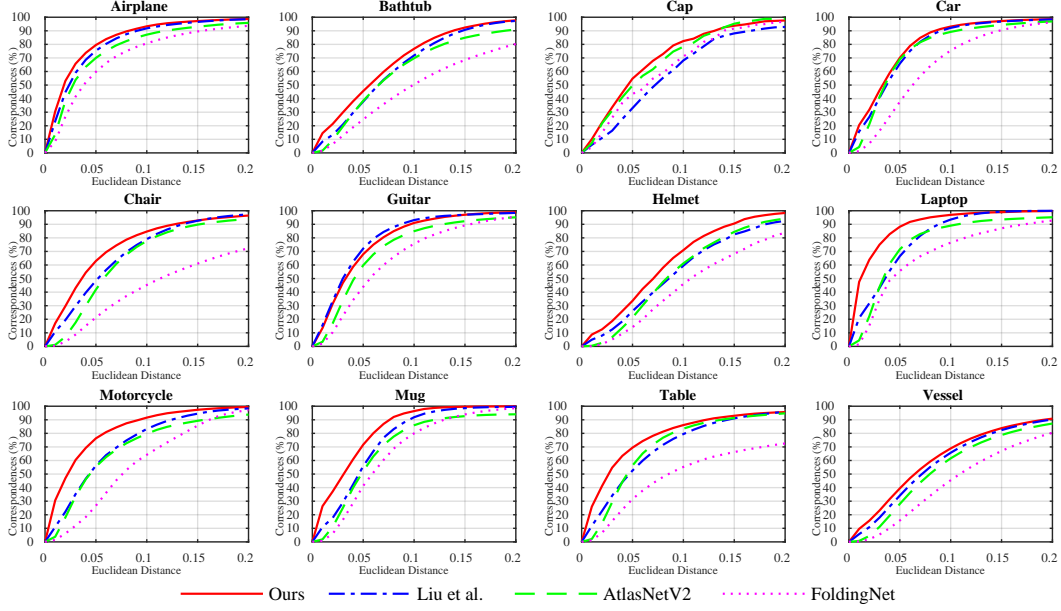


Figure 3: Correspondence accuracy for 12 categories in the KeypointNet dataset.

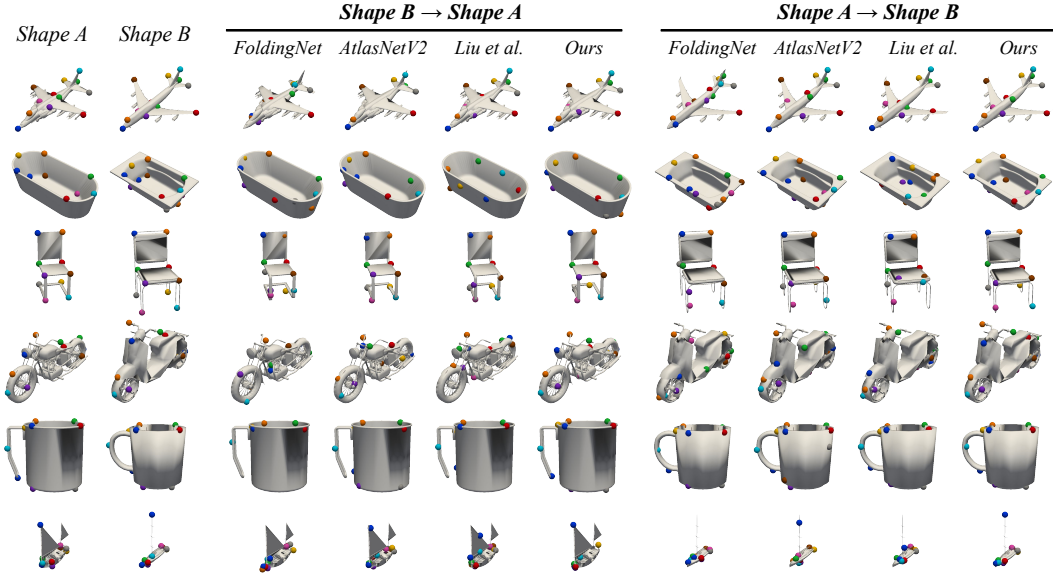


Figure 4: Keypoint transfer results for five categories: airplane, bathtub, chair, motorcycle, mug, and vessel. Each row contains two shape each with ground-truth keypoints and its pairwise transfer result.

as baselines. We then report quantitative and qualitative comparisons with these baselines for 3D semantic keypoint transfer and part segmentation label transfer. Finally, we present ablation studies to demonstrate the contribution of each component in the proposed model. More results can be found in the appendix. The source code will be made available to the public.

4.1 Experimental Setup

Dataset. We carry out the semantic keypoint transfer task on the KeypointNet dataset [30] as the BHCP benchmark used in Liu et al. [12] is not publicly available. Compared to the BHCP benchmark, the KeypointNet dataset is more challenging because: (a) it contains diverse objects and comes with large-scale annotations, (b) it is template-free and annotated by a large group of people, thus is less biased compared to the keypoints in the BHCP benchmark, which are from predefined templates.

	pla.	bag	cap	cha.	ear.	gui.	kni.	lam.	lap.	bik.	mug	pis.	roc.	ska.	tab.	avg.
Liu et al.	60.1	56.2	59.7	72.2	45.3	81.5	66.4	42.6	88.5	40.5	87.5	66.4	37.2	50.7	70.4	61.7
Ours	61.3	59.3	61.6	72.6	55.5	78.9	71.3	53.2	89.9	55.4	86.5	66.2	40.2	61.8	72.5	65.8

Table 1: Part label transfer results for 15 categories in the ShapeNet part dataset. Number measured with average IOU(%).

For the part segmentation label transfer task, we use the ShapeNet part dataset [31] as in [12]. For both datasets, we use the split provided in the original paper, and generate all pairs of shapes in the testing set as our testing pairs. To avoid interference from non-existing correspondences, we leave out instance pairs that do not share the same keypoint or part label. In all experiments, including our method and the baselines, we use a validation set for model selection.

Baselines. We evaluate the proposed method against state-of-the-art learning-based 3D dense correspondence prediction approaches, including AtlasNetV2 [18], FoldingNet [17], and Liu et al. [12]. Specifically, FoldingNet deforms from a fixed UV grid, while AtlasNetV2 explicitly allows the shape to be deformed from learnable elementary 3D structures. Neither of them estimates the confidence of correspondences. Liu et al. [12] propose a method that utilizes part features learned by the BAE-NET [11] to learn dense correspondence, including a mechanism that estimates the correspondence confidence.

Implementation Details. For both the point canonical mapping encoder and point inverse mapping decoder (see Figure 1), we follow [18] and use a three-layer MLP with ReLU activations, BatchNorm layers except for the last layer, where we use a hyperbolic tangent activation to obtain the final output. The training phase of our approach consists of two stages: (1) A pre-training stage trained with L_{ACD} (Eq. 1) and L_{rec} (Eq. 2) using $\alpha = 1$ for L_{ACD} (2) A fine-tuning stage trained with L_{ACD} , L_{rec} , and L_{cross} (Eq. 3) where we set $\alpha = 0$ for L_{ACD} . For all experiments, we set $k = 2048$, $\tau = 0.9$ (see Section 3.2), and the parameters of the network are optimized using the Adam [32] optimizer, with a constant learning rate of $1e^{-4}$.

4.2 3D Semantic Keypoints Transfer

For fair comparisons, we follow [12, 25] and compute the distances from transferred keypoints to ground truth keypoints and report the percentage of testing pairs where the distances are below a given threshold in Figure 3. We demonstrate that for 11 out of 12 categories (e.g. airplane, chair, mug, etc.), keypoints transferred via our learned correspondence are more accurate than other methods [12, 18, 17]. At the distance threshold of 0.05, our method performs 11.2% more accurately than Liu et al. [12] on average of all categories. Figure 3 demonstrates the qualitative results of the keypoint transfer task. Even for categories with large intra-class variation, e.g. bathtub, motorcycle, or vessel, our method is able to transfer keypoints accurately thanks to the learned dense correspondence.

4.3 Part Segmentation Label Transfer

We further validate our approach on the part label transfer task and present quantitative results in Table 1 and qualitative results in Figure 5. Note that the settings are different from that of Liu et al. [12], which directly utilizes the branched co-segmentation results for evaluation (thus different quantitative results between the Table 1 and that in their paper). In Table 1, we show the intersection-over-union (IoU) between transferred and ground truth part labels. Our method performs better than Liu et al. [12] in 12 out of 15 categories and has a higher average IoU. For categories with large intra-class variations, such as lamps, motorbikes, our approach significantly outperforms Liu et al. [12]. The performance difference is most likely due to the branched co-segmentation [11] adopted by Liu et al. [12]. Branched co-segmentation relies heavily on the size of training data available. Such an approach is vulnerable to large shape variations [11], and is unable to segment flat surfaces. Moreover, its performance is sensitive to the pre-defined number of branches. Instead, our method naturally links different instances through a canonical primitive and is thus more robust to large shape variations. We show the qualitative results in Figure 5. Thanks to the dense correspondence learned by the proposed method, we are able to transfer small parts more accurately such as the seat of a motorcycle (the green points) and the pipe of a lamp (the purple points) comparing to Liu et al. [12].

4.4 Correspondence Confidence

Given a source shape S_A and a target shape S_B , for every point $q \in S_B$, our model computes a confidence score indicating whether its corresponding point exists in S_A , as discussed in Section 3.2.

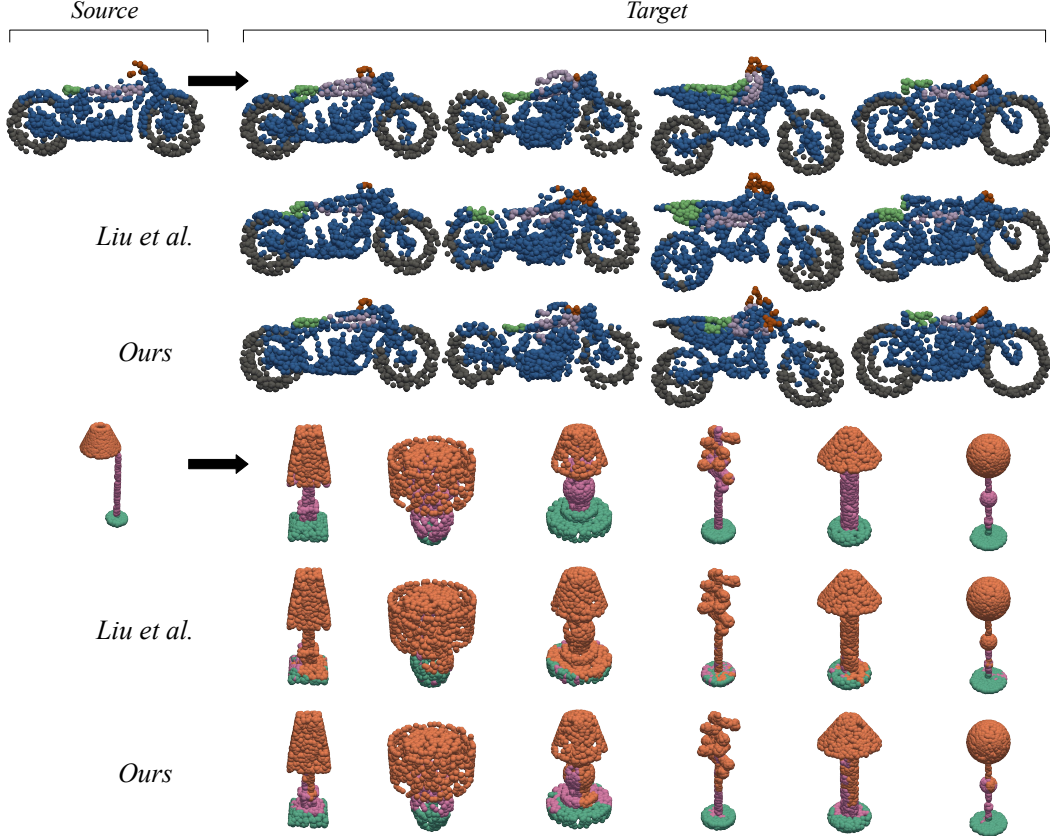


Figure 5: Qualitative results of part label transfer. The 1st row of the target indicates the ground truth instance part labels, while the rest shows the label transferring results via learned correspondences.

As annotations can be biased by the annotator’s definitions on keypoints, there is no absolute ground-truth for non-existence label between a shape pair. Thus, we visualize the confidence score as heatmaps for multiple target shapes in the airplane category in Figure 6 and compare with Liu et al. [12]. As shown in Figure 6, the proposed method is able to produce a more fine-grained confidence score compared to Liu et al. [12]. This is because our approach explicitly evaluates the confidence of correspondences at a more fine-grained level – the distance between points, instead of a distance at the part-level, as proposed in [12].

4.5 Ablation Studies

Effectiveness of cross-reconstruction. The cross-reconstruction architecture is designed to ensure that corresponding points overlapping as much as possible on the canonical space. In our experiments, we find that with the datasets containing shapes with aligned 6D poses [30, 10], a single branch encoder-decoder framework (i.e., w/o L_{cross}) already produces a reasonable prediction of correspondences. However, as shown in Figure 7 (red vs blue), our cross-reconstruction framework significantly improves the performance with a large margin.

In addition, we validate the effectiveness of the framework on un-aligned shapes, by rotating the input point cloud with radian noise $\mathcal{N}(0, 0.5^2)$. We note that all co-segmentation approaches assume that the pose of input shapes are consistently aligned [11, 12]. Consistent with the assumption, such rotation severely degrades the performance of Liu et al. [12] (brown line). In contrast, with the help of cross-reconstruction loss (orange line), our model is rotation-invariant to a certain degree.

Effectiveness of adaptive Chamfer loss. To show that the adaptive Chamfer loss is necessary, we train our model with constant $\alpha = 0$ and $\alpha = 1$, respectively. The results are shown in Figure 7. When α is set to zero consistently, the primitive would eventually condense to a single point in the canonical space, therefore, significantly hurts the performance (pink line). On the other hand, if

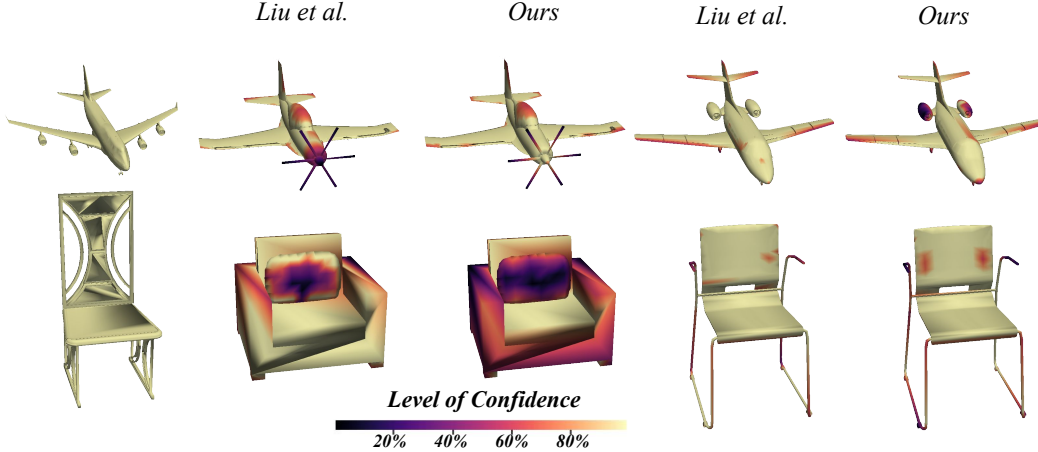


Figure 6: Heatmaps representing the correspondence confidence generated by our network. Source shape is in the leftmost of each row and dark color in each heatmap refers to low confidence in existing correspondence.

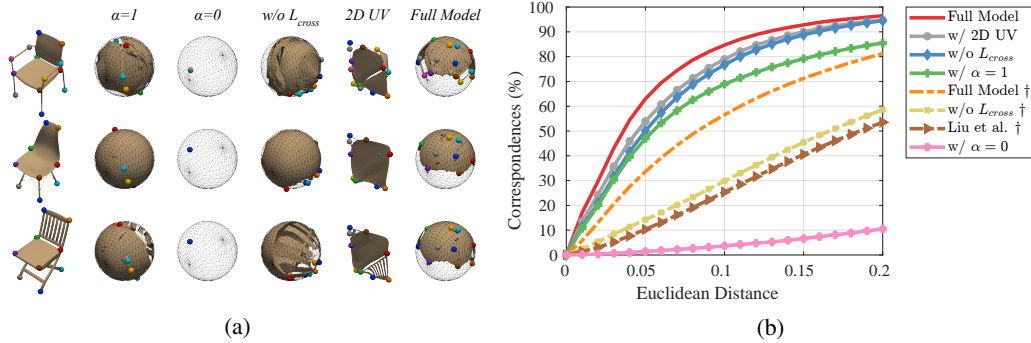


Figure 7: Qualitative (a) and quantitative (b) results of ablation studies on (i) the cross-reconstruction loss term (ii) the adaptive Chamfer loss term (iii) different types of canonical UV primitive using the chair category in the KeypointNet dataset. Note that the \dagger sign indicates methods trained with an un-aligned setting.

$\alpha = 1$, it is equivalent to enforce a single canonical primitive for all instances by encouraging the primitive to cover the entire canonical space. This ignores the intra-class variation and deteriorates the performance as shown in Figure 7 (green line).

Using a 2D UV grid vs. 3D UV sphere as a primitive. To analyze the effect of different canonical UV primitives, we further train our model using a 2D UV grid instead of a 3D UV sphere. Figure 7 shows that parameterizing the canonical space with a 3D sphere quantitatively outperforms a 2D grid (grey line). The main reason is that the sphere is continuous at any point while a 2D grid is discontinuous at boundaries.

5 Conclusions

In this work, we propose a self-supervised model, CPAE, that learns dense correspondence between 3D shapes in the same category. We introduce a canonical UV sphere, where dense correspondence for all the shapes can be explicitly obtained from. The key is to learn a 3D world coordinate to canonical space mapping, so that points from different instances are regarded as a pair of correspondences if they overlap on the sphere. We fulfill it through an autoencoder equipped with an adaptive Chamfer loss in the bottleneck, and a cross-reconstruction structure in the decoder. Experimental results validate the proposed method performs favorably against state-of-the-art schemes in various tasks and ablations. We show that our model is much more rotation-invariant than the existing approaches.

Appendix

In the Appendix, we provide:

- ◇ Application on texture transfer in Section 6.
- ◇ The computational time and model size of our approach in Section 7.
- ◇ Qualitative results of instance-aware primitives in Section 8.
- ◇ Qualitative results of part label transfer in Section 9.
- ◇ Correspondence Confidence Heatmap Visualization in Section 10.
- ◇ Limitation and failure cases in Section 11.

6 Application on Texture Transfer

Given a source 3D shape, we transfer texture from the source shape to multiple target shapes using computed correspondences. Our method is able to detect points that do not have correspondents in the source 3D shape (e.g., airplane without tail wings or stabilizers).



Figure 8: Applications on texture transfer.

7 Computational Time and Model Size

7.1 Training Details

We use the chair category as an example to illustrate the training pipeline. With 500 training samples, the training takes about 24 hours to converge, (4 hours for stage one ($\alpha = 1$) and 20 hours for stage two ($\alpha = 0$)), on a single Tesla V100 GPU. Please see Algorithm 1 and Section 4.1 in the main paper for more details on the two stage training paradigm. *The source code will be released to public upon publication.*

Algorithm 1 : The training phase of our approach consists of two stages: (1) A pre-training stage trained with L_{ACD} and L_{rec} (2) A fine-tuning stage trained with L_{ACD} , L_{rec} , and L_{cross}

(A) STAGE-1: PRE-TRAINING

▷ 4 hours on Chair category

- 1: Randomly sub-sample k points from the input point cloud S_A ;
- 2: Initialize weight of the global feature encoder $E(\cdot)$, canonical mapping encoder $\Phi(\cdot)$ and inverse mapping decoder $\Psi(\cdot)$;
- 3: **for** epoch **in range** [0,T] **do**
- 4: **foreach** iteration **do**
- 5: $z_A \leftarrow E(S_A)$;
- 6: $U_A \leftarrow \Phi([p, z_A])$, where $p \in S_A$;
- 7: $\hat{S}_{A \rightarrow A} \leftarrow \Psi([q, z_A])$, where $q \in U_A$;
- 8: Obtain loss L_{ACD} ($\alpha = 1$) and L_{rec} ;
- 9: Update weight;

(B) STAGE-2: FINE-TUNING

▷ 20 hours on Chair category

- 1: Generate randomly paired samples S_A and S_B ;
- 2: **while** not converged **do**
- 3: **foreach** iteration **do**
- 4: $z_A \leftarrow E(S_A)$;
- 5: $U_A \leftarrow \Phi([p, z_A])$, where $p \in S_A$;
- 6: $\hat{S}_{A \rightarrow A} \leftarrow \Psi([q, z_A])$, where $q \in U_A$;
- 7: Obtain loss L_{ACD} ($\alpha = 0$) and L_{rec} ;
- 8: $z_B \leftarrow E(S_B)$;
- 9: $U_B \leftarrow \Phi([p, z_B])$, where $p \in S_B$;
- 10: $\hat{S}_{A \rightarrow B} \leftarrow \Psi([q, z_B])$, where $q \in U_A$;
- 11: $\hat{S}_{B \rightarrow A} \leftarrow \Psi([q, z_A])$, where $q \in U_B$;
- 12: Obtain loss L_{cross} ;
- 13: Update weight;

7.2 Inference Details

Please see Figure 9 and Section 3.2 in the main paper for more details on the inference pipeline. Our proposed CPAE model contains 2.07M parameters which is $2.5 \times$ less than the 5.22M parameters in [12]. At inference time, the computational time for label transfer between a pair of shapes (each with 2048 points) is 0.03 second including runtimes of the nearest neighbor search for both shapes.

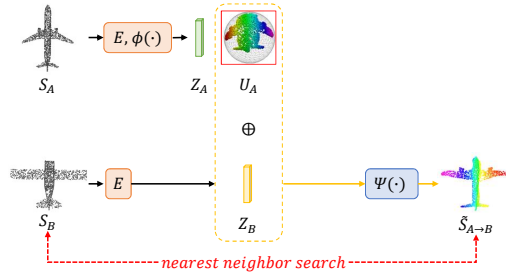


Figure 9: The inference flow of our approach.

8 Qualitative Results of Instance-aware Primitives

In Figure 10, we demonstrate more examples of the instance-aware primitives as discussed in Section 3.1 in the main paper. Two observations can be made from this figure: a) The instance-aware primitives produced by our canonical mapping are closely adhered to a canonical sphere. b) points of the same semantic parts are mapped to nearby locations on the primitives, as shown by the colored keypoints in Figure 10. These observations demonstrate that our model is able to learn correspondence across different shapes in the same category.

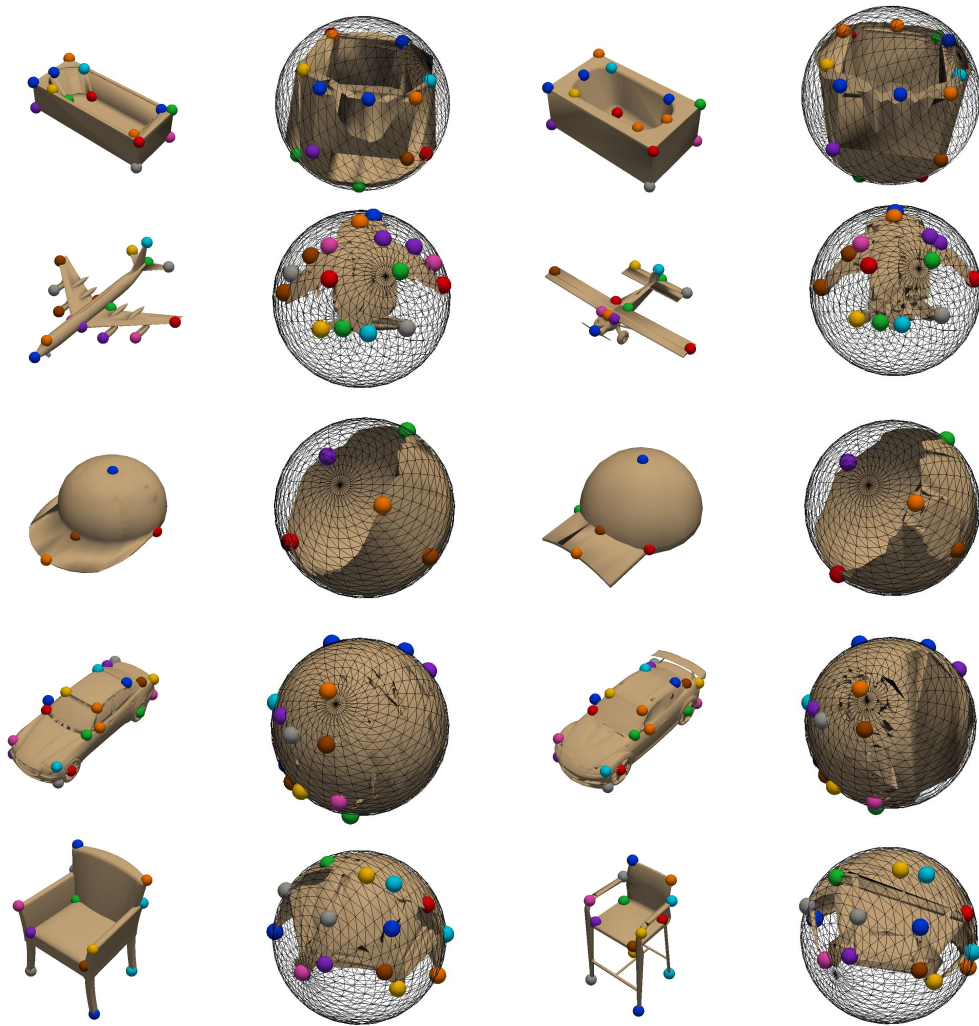


Figure 10: Instance-aware primitives on five different categories from the KeypointNet dataset [30]

9 Qualitative Results of Part Label Transfer

In Figure 11, we show more qualitative results of the part label transfer task. Thanks to the dense correspondences learned by our model, we can transfer part labels for small parts (e.g. the handle of mugs or the tail wings of airplanes) and handle large intra-class variations (e.g. different legs of chairs in row three in Figure 11).

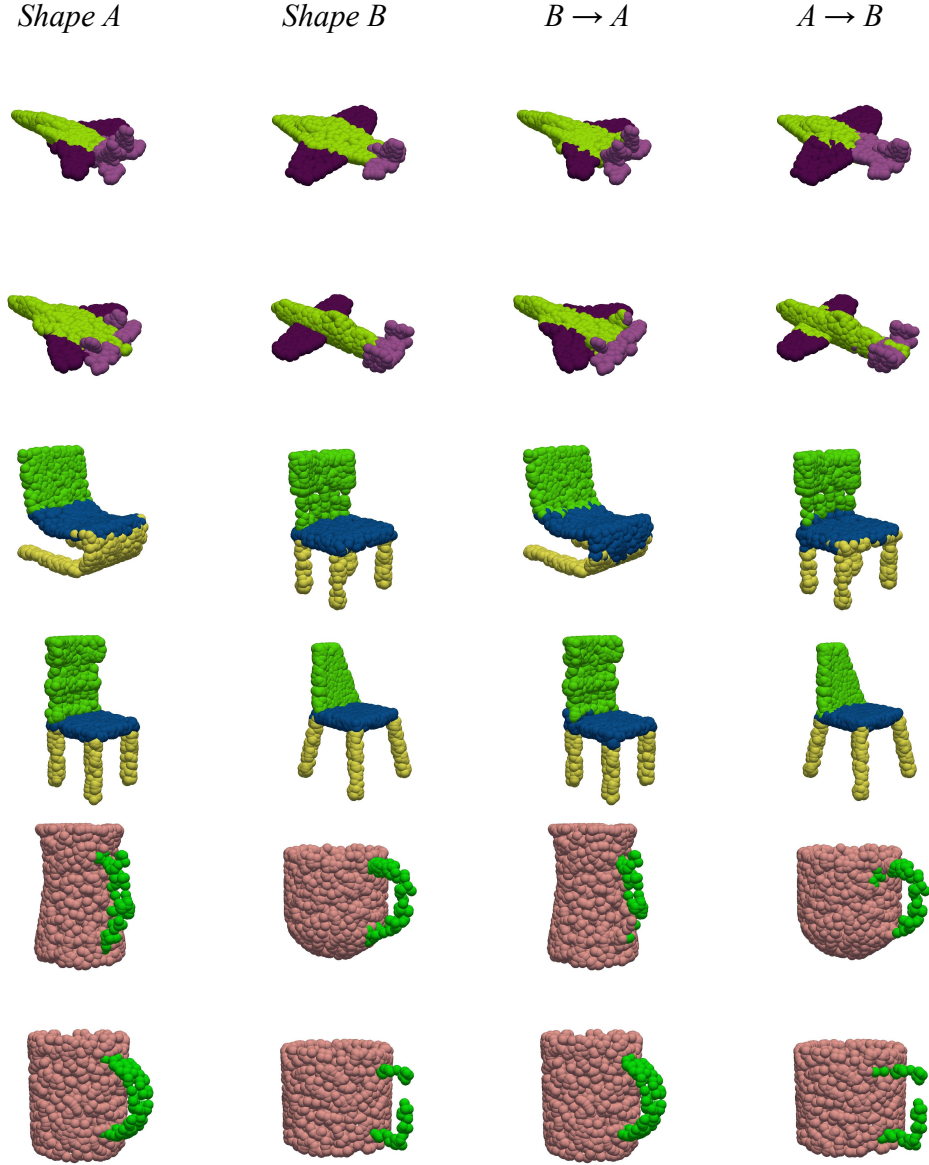


Figure 11: Part label transfer results. $B \rightarrow A$ refers to transferring shape B’s label to shape A.

10 Correspondence Confidence Heatmap Visualization

We use the confidence score (mentioned in main paper Section 3.4) to draw heatmaps for multiple target shapes in the same categories. As shown in Figure 12, the predicted confidence heat maps successfully indicate the intra-class variations and capture uncertainty in correspondence prediction. For instance, low confidences can be found in mugs with different handles, knives with different blades, guitars with different bodies, etc.

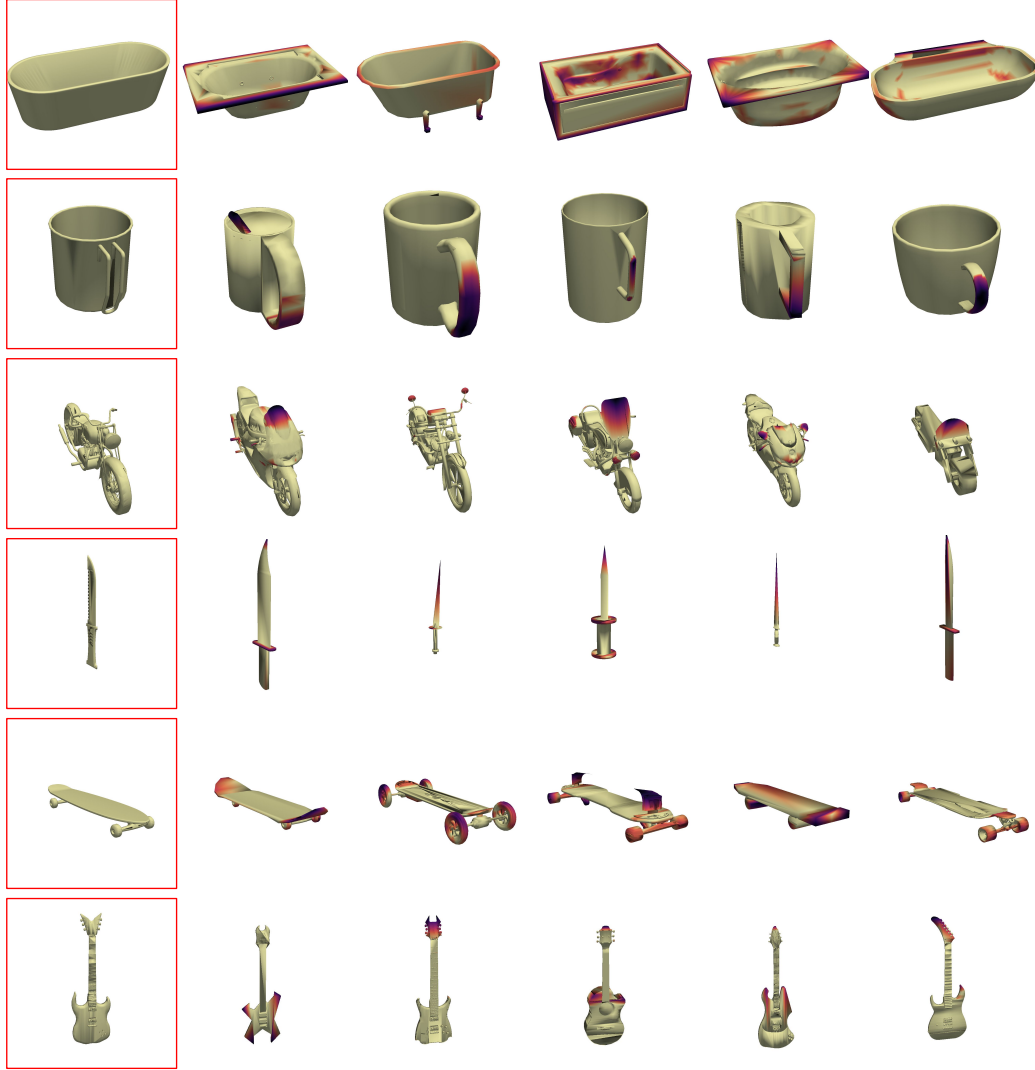


Figure 12: Correspondence confidence heatmaps. Red boxes indicate source shapes. The darker the heatmap, the lower the confidence.

11 Limitation

There are two main limitations for our approach: (a) we encode the shape information of a point cloud in a global vector – i.e., fine details like corners and edges may be blurred after reconstruction. (b) We found the correspondences predicted near holes maybe wrong, possibly due to the sparsity of points in the point cloud and the nature of Chamfer and Earth Mover’s distance matrices. We leave these limitations for future works.

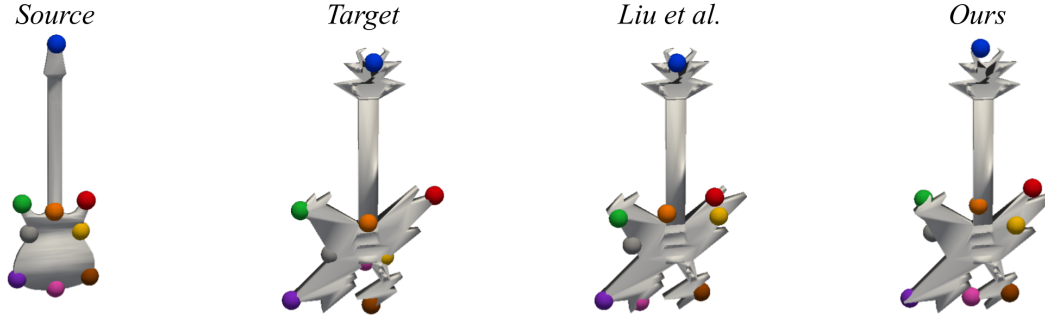


Figure 13: Failure cases.

References

- [1] Ashutosh Saxena, Justin Driemeyer, Justin Kearns, and Andrew Y Ng. Robotic grasping of novel objects. In *NIPS*, pages 1209–1216, 2007. [1](#)
- [2] Andrew T Miller, Steffen Knoop, Henrik I Christensen, and Peter K Allen. Automatic grasp planning using shape primitives. In *ICRA*, pages 1824–1829, 2003. [1](#)
- [3] Qiang Hao, Rui Cai, Zhiwei Li, Lei Zhang, Yanwei Pang, Feng Wu, and Yong Rui. Efficient 2d-to-3d correspondence filtering for scalable 3d object recognition. In *CVPR*, pages 899–906, 2013. [1](#)
- [4] Wang Zeng, Wanli Ouyang, Ping Luo, Wentao Liu, and Xiaogang Wang. 3d human mesh regression with dense correspondence. In *CVPR*, pages 7054–7063, 2020. [1](#)
- [5] Xueting Li, Sifei Liu, Kihwan Kim, Shalini De Mello, Varun Jampani, Ming-Hsuan Yang, and Jan Kautz. Self-supervised single-view 3d reconstruction via semantic consistency. In *ECCV*, 2020. [1](#), [3](#)
- [6] Angjoo Kanazawa, Shubham Tulsiani, Alexei A. Efros, and Jitendra Malik. Learning category-specific mesh reconstruction from image collections. In *ECCV*, 2018. [1](#)
- [7] Abhishek Badki, Orazio Gallo, Jan Kautz, and Pradeep Sen. Meshlet priors for 3d mesh reconstruction. In *Proceedings of the IEEE/CVF Conference on Computer Vision and Pattern Recognition*, pages 2849–2858, 2020. [1](#)
- [8] Thibault Groueix, Matthew Fisher, Vladimir G Kim, Bryan C Russell, and Mathieu Aubry. 3d-coded: 3d correspondences by deep deformation. In *ECCV*, pages 230–246, 2018. [1](#), [3](#)
- [9] Syed Zulqarnain Gilani, Ajmal Mian, Faisal Shafait, and Ian Reid. Dense 3d face correspondence. *IEEE TPAMI*, 40(7):1584–1598, 2017. [1](#)
- [10] Angel X Chang, Thomas Funkhouser, Leonidas Guibas, Pat Hanrahan, Qixing Huang, Zimo Li, Silvio Savarese, Manolis Savva, Shuran Song, Hao Su, et al. Shapenet: An information-rich 3d model repository. *arXiv preprint arXiv:1512.03012*, 2015. [1](#), [8](#)
- [11] Zhiqin Chen, Kangxue Yin, Matthew Fisher, Siddhartha Chaudhuri, and Hao Zhang. Bae-net: Branched autoencoder for shape co-segmentation. In *CVPR*, pages 8490–8499, 2019. [1](#), [2](#), [7](#), [8](#)
- [12] Feng Liu and Xiaoming Liu. Learning implicit functions for topology-varying dense 3d shape correspondence. In *NeurIPS*, 2020. [1](#), [2](#), [5](#), [6](#), [7](#), [8](#), [11](#)
- [13] Angjoo Kanazawa, Shubham Tulsiani, Alexei A Efros, and Jitendra Malik. Learning category-specific mesh reconstruction from image collections. In *ECCV*, 2018. [1](#), [3](#)
- [14] Shubham Goel, Angjoo Kanazawa, , and Jitendra Malik. Shape and viewpoints without keypoints. In *ECCV*, 2020. [1](#), [3](#)
- [15] Shubham Tulsiani, Nilesh Kulkarni, and Abhinav Gupta. Implicit mesh reconstruction from unannotated image collections. *arXiv preprint arXiv:2007.08504*, 2020. [1](#), [3](#)
- [16] Charles R Qi, Hao Su, Kaichun Mo, and Leonidas J Guibas. Pointnet: Deep learning on point sets for 3d classification and segmentation. In *CVPR*, pages 652–660, 2017. [2](#), [3](#)
- [17] Yaoqing Yang, Chen Feng, Yiru Shen, and Dong Tian. Foldingnet: Point cloud auto-encoder via deep grid deformation. In *CVPR*, pages 206–215, 2018. [2](#), [4](#), [5](#), [7](#)
- [18] Theo Deprelle, Thibault Groueix, Matthew Fisher, Vladimir Kim, Bryan Russell, and Mathieu Aubry. Learning elementary structures for 3d shape generation and matching. In *NeurIPS*, pages 7433–7443, 2019. [2](#), [3](#), [7](#)
- [19] Thibault Groueix, Matthew Fisher, Vladimir G Kim, Bryan C Russell, and Mathieu Aubry. A papier-mâché approach to learning 3d surface generation. In *CVPR*, pages 216–224, 2018. [2](#), [3](#)
- [20] Guandao Yang, Xun Huang, Zekun Hao, Ming-Yu Liu, Serge Belongie, and Bharath Hariharan. Pointflow: 3d point cloud generation with continuous normalizing flows. In *ICCV*, 2019. [2](#)
- [21] Mingjia Chen, Qianfang Zou, Changbo Wang, and Ligang Liu. Edgenet: Deep metric learning for 3d shapes. *Computer Aided Geometric Design*, 72:19–33, 2019. [2](#)
- [22] Christopher Choy, Jaesik Park, and Vladlen Koltun. Fully convolutional geometric features. In *ICCV*, pages 8958–8966, 2019. [2](#)

- [23] Zan Gojcic, Caifa Zhou, Jan D Wegner, and Andreas Wieser. The perfect match: 3d point cloud matching with smoothed densities. In *CVPR*, pages 5545–5554, 2019. [2](#)
- [24] Bharat Lal Bhatnagar, Cristian Sminchisescu, Christian Theobalt, and Gerard Pons-Moll. Combining implicit function learning and parametric models for 3d human reconstruction. In *ECCV*, 2020. [2](#)
- [25] Nenglu Chen, Lingjie Liu, Zhiming Cui, Runnan Chen, Duygu Ceylan, Changhe Tu, and Wenping Wang. Unsupervised learning of intrinsic structural representation points. In *CVPR*, pages 9121–9130, 2020. [2](#), [7](#)
- [26] Jeong Joon Park, Peter Florence, Julian Straub, Richard Newcombe, and Steven Lovegrove. DeepSDF: Learning continuous signed distance functions for shape representation. In *CVPR*, 2019. [5](#)
- [27] Lars Mescheder, Michael Oechsle, Michael Niemeyer, Sebastian Nowozin, and Andreas Geiger. Occupancy networks: Learning 3d reconstruction in function space. In *CVPR*, pages 4460–4470, 2019. [5](#)
- [28] Vincent Sitzmann, Michael Zollhöfer, and Gordon Wetzstein. Scene representation networks: Continuous 3d-structure-aware neural scene representations. In *NeurIPS*, 2019. [5](#)
- [29] Ben Mildenhall, Pratul P. Srinivasan, Matthew Tancik, Jonathan T. Barron, Ravi Ramamoorthi, and Ren Ng. Nerf: Representing scenes as neural radiance fields for view synthesis. In *ECCV*, 2020. [5](#)
- [30] Yang You, Yujing Lou, Chengkun Li, Zhoujun Cheng, Liangwei Li, Lizhuang Ma, Cewu Lu, and Weiming Wang. Keypointnet: A large-scale 3d keypoint dataset aggregated from numerous human annotations. In *CVPR*, pages 13647–13656, 2020. [6](#), [8](#), [12](#)
- [31] Li Yi, Vladimir G Kim, Duygu Ceylan, I-Chao Shen, Mengyan Yan, Hao Su, Cewu Lu, Qixing Huang, Alla Sheffer, and Leonidas Guibas. A scalable active framework for region annotation in 3d shape collections. *ACM TOG*, 35(6):1–12, 2016. [7](#)
- [32] Diederik P Kingma and Max Welling. Auto-encoding variational bayes. *arXiv preprint arXiv:1312.6114*, 2013. [7](#)